

# Chemical nonequilibrium effects in the wake of a boundary-layer sized object in hypersonic flows

By M. Birrer<sup>†</sup>, C. Stemmer<sup>†</sup>, G. Groskopf<sup>‡</sup> AND M. Kloker<sup>‡</sup>

The hypersonic boundary-layer flow around and in the wake of a cuboid obstacle in the size of the order of half the boundary-layer height under the influence of chemical non-equilibrium as it is present during (re-)entry scenarios is presented here. This is demanding the consideration of hot flow conditions as they are present during re-entry from space but cannot be reproduced in wind tunnels. The wake of the object delivers hot gas from within the boundary layer onto the colder surface, which can lead to increased ablation and, as a worst-case-scenario, to the failure of the underlying TPS (thermal protection system). The influence of the chemical non-equilibrium on these complex flows is yet unknown and represents the focal point of the investigation during the Summer Program.

A second effect, which can be even more dramatic, is the change in stability characteristics by the wake and possible transition to turbulent flow downstream of the protruding obstacle, which can lead to an increase in heat transfer by a factor of 10 for hypersonic flows.

The purpose of the investigation is to shed light on the role of chemical non-equilibrium in hypersonic flows around obstacles in the size of the boundary-layer thickness (i.e., mounts). The flow conditions are high Mach number and hot flow since this is not attainable in wind tunnels and calculations need to be employed for further insight.

The geometric setup is chosen in accordance to the setup of the HyBoLT experiment investigated by NASA. First, 2-D DNS for caloric perfect gas, chemical equilibrium and non-equilibrium deliver the inflow and free stream conditions for detailed 3-D steady DNS around the obstacle including the wake. The presented investigations show the change in recirculation lengths and the change in temperatures in the wake for the three flow conditions for a flight Mach number of 8.5, which is the highest speed to be measured by the HyBoLT experiment. Stability calculations complement the evaluation of chemical reactions on the flow characteristics.

## 1. Introduction

Returning space-traveling vehicles are always exposed to extreme heat loads during reentry and therefore require the design of a sufficient heat shield to protect the underlying structure from damage. The return of the space shuttle Columbia in 2003 sadly demonstrated the impact a malfunctioning heat shield can have.

Post-flight investigations on returned capsules have shown that the flow around the stagnation point could be predicted quite well with quasi-steady methods, while along the heat shield, predictions can be significantly different to reality. Former ways to deal

<sup>†</sup> Lehrstuhl für Aerodynamik, Technische Universität München, Boltzmannstr. 15, 85748 Garching b. München, Germany

<sup>‡</sup> Institut für Aero- und Gasdynamik, Universität Stuttgart, Pfaffenwaldring 21, 70550 Stuttgart, Germany

with this were to assume turbulent flow over the entire surface and add a considerable safety factor. This of course results in a major decrease of payload capacities. Having in mind the cost per mass sent out to space makes this an unacceptable approach for today's projects.

Recent plans of manned flights back to the moon and at later stages to Mars arouse interest regarding understanding effects of boundary-layer flows with dissociation and non-equilibrium excitation of vibrational degrees of freedom. High temperatures make it necessary to consider chemical reactions while the very high speed can call for non-equilibrium models. Ablation of the shield adds another degree of complexity to the system, changing the fluid composition, energy distribution as well as the shape of the surface (which is not considered in this work).

Recent experimental efforts (Schneider 2007; Tirtley *et al.* 2008; Berry & Horvath 2007, among others) have been undertaken to investigate the influence of roughness on hypersonic transition where roughness usually describes a small wall-normal extension compared to the local boundary-layer thickness. Bigger-sized objects, so-called obstacles, show considerable changes in the wall heat transfer downstream. Free-flight conditions matching all relevant characteristic scales (in particular the Damköhler number) cannot be attained in the wind tunnels and free-flight experiments are extremely difficult to undertake with respect to controlled conditions and accurate measurements required for transition research. Therefore, numerical investigation for flight conditions have to complement these experimental investigations. Receptivity analysis has recently been presented by Wang & Zhong (2008), but only for ideal gas.

The focus of this paper is on the effects of chemical reactions and non-equilibrium conditions in a boundary-layer flow with an obstacle. We will compare the flow around a surface-mounted object by means of three different chemical and non-equilibrium models. The results from a caloric perfect gas model will be compared with results from chemically reacting flows in thermal and chemical equilibrium. Finally, chemical non-equilibrium will be evaluated and compared to the aforementioned results.

Secondary stability calculations by G. Groskopf and M. Kloker give some preliminary insight to the change in amplification rates due to the change in steady base flow in the presence of chemical reactions.

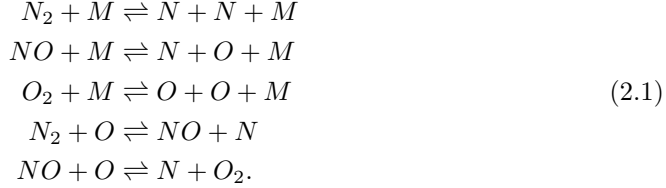
## 2. Numerical method

### 2.1. Governing equations

We are solving the complete compressible Navier Stokes equations in multiple blocks using MPI, hence the name of the software NSMB (Navier Stokes Multi Block; see Vos *et al.* 2006,2007). The package uses higher-order finite differences to solve the equations with explicit (Runge-Kutta) or implicit time integration. The grid can be chosen appropriate to the geometry as generalized coordinates are used. Appropriate boundary conditions (non-reflecting at the free-flow surface) are used.

Three different cases will be investigated: caloric perfect gas model, chemically reacting flow (air) in equilibrium and chemical non-equilibrium. The latter two models are both five species models by Park (Park 1985). The species are  $N$ ,  $NO$ ,  $N_2$ ,  $O$  and  $O_2$ . The chemical model is valid up to 9000 Kelvin. For the equilibrium model, the equilibrium constants are calculated to minimize the Gibbs free energy. The non-equilibrium model calculates the concentrations by solving seventeen reaction equations (three dissociation reactions with any collision partner and two recombination reactions), shown in Eq. (2.1).

Here,  $M$  stands for any one of the five species:



For the caloric perfect gas model, viscosity is calculated by Sutherland's law, given by Eq. (2.2), where  $\mu_\infty$  represents the viscosity at the reference temperature  $T_\infty$  and  $S_1 = 110.3\text{K}$ .

$$\frac{\mu}{\mu_\infty} = \left(\frac{T}{T_\infty}\right)^{3/2} \frac{T_\infty + S_1}{T + S_1} \tag{2.2}$$

The two models using chemical reactions use the Blottner model to obtain the viscosity and thermal conductivity of each species (Eq. (2.3), see also Blottner 1970). The mixture viscosity is calculated by Wilke's semi-empirical relation (Bird *et al.* 1960), given by Eq. (2.4).

$$\mu_s = 0.1 \cdot \exp[(A_s \ln(T) + B_s) \ln(T) + C_s] \tag{2.3}$$

$$\mu_{mix} = \sum_s \left( \frac{X_s \mu_s}{\sum_s X_r \phi_{sr}} \right) \tag{2.4}$$

where

$$\Phi_{sr} = \frac{1}{\sqrt{8}} \left(1 + \frac{M_s}{M_r}\right)^{-1/2} \left[1 + \left(\frac{\mu_s}{\mu_r}\right)^{1/2} \left(\frac{M_r}{M_s}\right)^{1/4}\right]^2 \tag{2.5}$$

NSMB allows for simulations with thermal non-equilibrium, which is not considered in this work.

### 3. Simulations

#### 3.1. Geometry

We decided to investigate the geometry of the NASA HyBoLT flight experiment (see Berry *et al.* 2007) to allow for later comparison with free-flight results. The experiment consists of a wedge with a half angle of six° mounted on top of a rocket to be launched Aug. 22 2008. The leading edge has a radius of 3.81 mm, which puts it 32.64 mm behind a virtual sharp leading edge. The focus of our investigation was a cubical-shaped obstacle located 508 mm from the virtual leading edge. Unlike the obstacle for the flight experiment it is aligned with the flow. The height is chosen to the prediction from Berry *et al.* (2007) for the conditions in the Mach 8.5 case, which is supposed to be the highest of available measurements. The length and the width are set to twice the height. Figure 1 shows a 2-D sketch of the setup.

#### 3.2. Freestream conditions

We decided to use the Mach 8.5 conditions of the predicted trajectory of the HyBoLT flight experiment given in Berry *et al.* (2007) because it was the highest velocity measured promising the largest effect from non-equilibrium. The given freestream values were therewith an altitude of 42.5 km, a velocity of 2732.6 m/s and a Reynolds number of

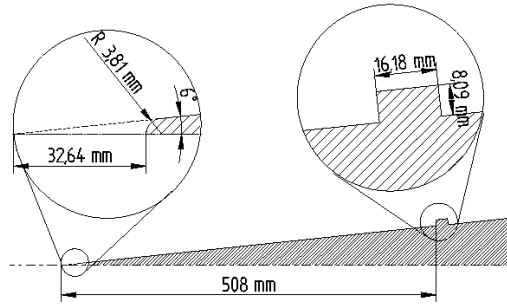


FIGURE 1. Sketch of our 2-D geometry used in the study, based on the HyBoLT design (Berry et al. 2007). In 3-D the spanwise dimension of the obstacle is equal to the streamwise size.

$4.66 \cdot 10^5$  per meter. The temperature and density values for the freestream were calculated using the 1976 Standard Atmosphere to  $T_0=258.1$  K and  $\rho_0 = 2.78 \cdot 10^{-3}$  kg/m<sup>3</sup>.

### 3.3. Computational grids

The simulation is conducted in two stages. In a first stage, the whole 2-D geometry is simulated with a shock-capturing numerical scheme to obtain the appropriate conditions after the bow shock around the obstacle as freestream and inflow conditions for a detailed 3-D simulation around the obstacle for the different chemical models used. The grids for our two dimensional simulations were built up of 16 blocks, with two for the front edge. The blocks at the surface have cells with half the edge size of the outer blocks. It contains a total of  $2.1 \cdot 10^5$  finite volume cells. This gives us 16 cells for the obstacle height, and therefore 32 for the obstacle length.

The simulations on the 3-D grid were done on a reduced domain around the obstacle with increased resolution. The domain size is around 13 times the obstacle length in flow direction and 7 times in spanwise direction. The height is about 7 times the obstacle height. The grid consisted of 35 blocks of rectilinear submeshes. They summed up to have approximately 11 million cells. The resolution around the obstacle is 32 cells to capture the obstacle height and 64 for the length. The obstacle height corresponded to roughly 30% of the local boundary-layer thickness.

## 4. Results of direct numerical simulations

### 4.1. 2-D results

The 2-D simulation results show the expected decrease in temperature in the heated boundary layer under consideration of chemical reactions. Disregarding the area in front of the bow shock, we get a decrease in maximum temperature from 1913 K in the caloric case to around 1769 K in the equilibrium case. Figure 2 shows the temperature as a function of wall distance taken at a position 340 mm behind the leading edge. We see, that considering chemistry gives us a reduction of around 50 K in the peak temperature. The profiles in Fig. 2 are upstream of the recirculation zone and are the ones used as input for the 3-D calculation.

Also shown in Fig. 2 is the fact that, while the model with chemical equilibrium just gives reduced temperatures keeping a similar shape and the peak at the same height, the non-equilibrium case also shifts the peak closer to the surface. That, inter alia, means, that higher temperature gradients occur, leading to an increased heat flux to the surface and therefore higher strains on the heat shield.

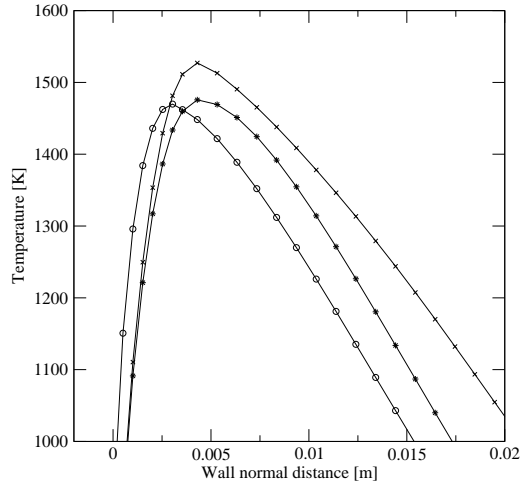


FIGURE 2. Temperature as a function of the wall-normal distance. The data is from the 2-D simulations of the different gas models, starting at the surface point at  $x=0.34\text{m}$ .  $\times$  is from the caloric model,  $*$  from the equilibrium and  $\circ$  the non-equilibrium gas model. These are results obtained by the 2-D simulation.

Figure 3 shows a contour plot of zero streamwise velocity to compare the lengths of the recirculation zones with different gas models. We can see that the equilibrium case has a slightly smaller zone than the caloric one. When switching to non-equilibrium chemistry, there is a significant reduction in recirculation length before and after the obstacle.

Table 1 shows concentrations of the different species from the various cases in 2-D and 3-D. The values of the reaction products  $N$ ,  $NO$  and  $O$  are maxima, while those of  $N_2$  and  $O_2$  are minima. As the main interest is the flow around and behind the obstacle, only the area behind the shock in the two dimensional case is considered in this comparison. The largest concentration of our products is 0.47 percent for  $NO$ , when we assume equilibrium chemistry. With non-equilibrium effects, the value is even smaller.

#### 4.2. 3-D results

The 3-D results show the same tendencies in temperature development and species concentrations as the 2-D results have indicated. When considering chemistry, the peak temperatures drop. But while assuming equilibrium chemistry gives us a significant temperature drop, the non-equilibrium case causes a smaller reduction compared to the caloric case. Also, the peak temperature moves toward the surface in the non-equilibrium case and can therefore result in normal surface temperature gradients, that can even exceed those of the caloric case. The differences between the recirculation zones do not seem to be as significant as they are in the two dimensional simulations. The species concentrations of the reaction products, shown in Table 1, are somewhat higher compared to the values obtained in the 2-D simulations, but are still small.

The main focus of the simulations is the 3-D flow in the wake of the obstacle. Figure 4 shows three planes, one for each direction, all containing the point of maximal temperature in the wake. The data is taken from the simulation with equilibrium chemistry. In the  $yz$ -plane at the top, we see, that there is a mushroom shaped area in the direct wake of the obstacle formed by two counter-rotating vortices. Two areas of maximum temperatures are found close to the center. The downstream development of the horse-shoe

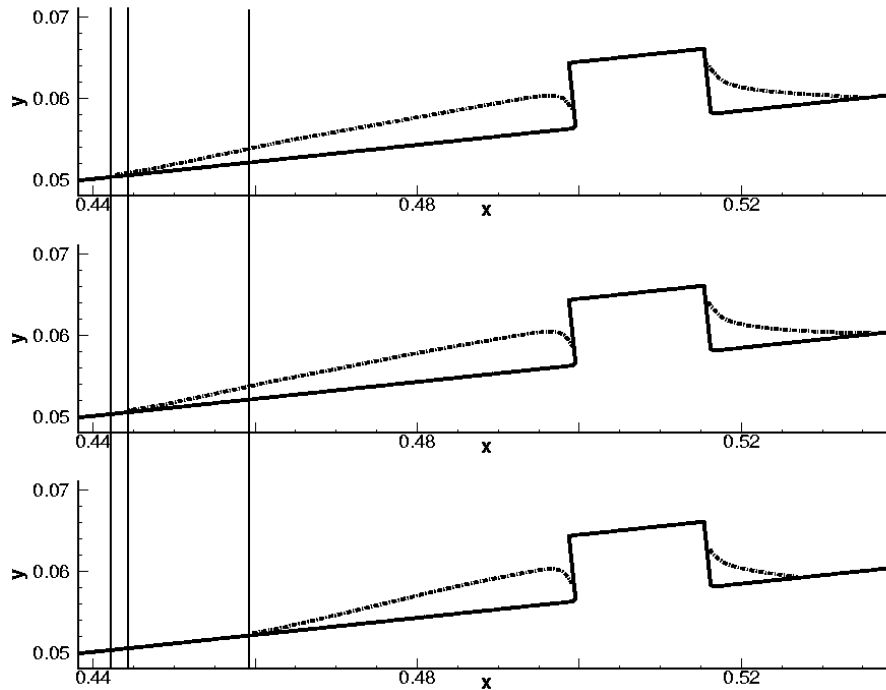


FIGURE 3. Comparison of the recirculation zone of the different gas models. The three plots show the zero  $u$  velocity contour of the caloric case at the top, the equilibrium case in the middle and the non-equilibrium at the bottom. The vertical lines are to mark the beginning of the recirculation zones.

vortex far outward from the center does not play a role since the maximum temperatures are far lower than in the direct wake of the object. Therefore, the center part of the wake is the area of main interest. For the case with non-equilibrium chemistry, shown in figure 5, this area is also where the concentration of reaction products  $N$ ,  $O$ ,  $NO$  are highest, whereas assuming equilibrium, the highest concentrations are located in front of the obstacle, where the maximal temperatures occur. The wall distance of the maximum temperature is increasing downstream as can be seen in the  $xz$ -view of figures 4 and 5. When we compare the two figures, we see, that in the case of non-equilibrium chemistry the peak temperature moves closer to the surface and closer to the obstacle causing higher heat fluxes to the obstacle, as well as to the surface. Also the counter-rotating vortices move closer together. Therefore the wall distance of the maximum temperature increases slightly faster downstream than in the equilibrium case.

## 5. Stability analysis

A biglobal linear stability analysis has been carried out using the eigenvalue solver described in Groskopf *et al.* (2008) assuming a calorically perfect or a reactive gas in chemical equilibrium, respectively. As the current version of the stability solver assumes the primary state to be a calorically perfect-gas flow with constant Prandtl number ( $Pr = 0.72$ ) and ratio of heat capacities ( $\kappa = 1.4$ ) without any chemical reactions, the analysis is fully appropriate only for the first flowfield to be investigated. For the second

Species	Chemical Equilibrium		Chemical Non-Equilibrium	
	2-D	3-D	2-D	3-D
$N$	$9.26 \cdot 10^{-11}$	$1.29 \cdot 10^{-7}$	$6.87 \cdot 10^{-12}$	$4.06 \cdot 10^{-10}$
$NO$	$4.79 \cdot 10^{-3}$	$1.70 \cdot 10^{-2}$	$2.96 \cdot 10^{-7}$	$1.35 \cdot 10^{-6}$
$N_2$	$7.65 \cdot 10^{-1}$	$7.59 \cdot 10^{-1}$	$7.67 \cdot 10^{-1}$	$7.67 \cdot 10^{-1}$
$O$	$2.59 \cdot 10^{-4}$	$7.77 \cdot 10^{-3}$	$4.15 \cdot 10^{-5}$	$4.09 \cdot 10^{-5}$
$O_2$	$2.30 \cdot 10^{-1}$	$2.16 \cdot 10^{-1}$	$2.33 \cdot 10^{-1}$	$2.33 \cdot 10^{-1}$

TABLE 1. Species concentrations of the different models from the 2-D and 3-D simulations. As our interest in this work is not in the area around the leading edge, for the 2-D cases only values behind the shock are considered. For  $N$ ,  $NO$  and  $O$ , being the reaction products, the maximal values are given, for  $O_2$  and  $N_2$  it is the minimal concentration.

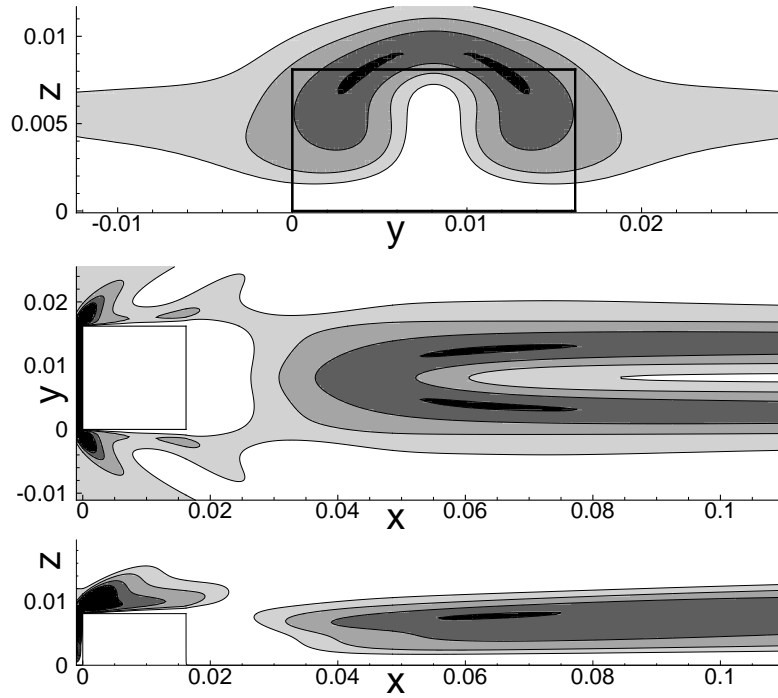


FIGURE 4. Contour plot of the temperature shown in three planes cutting through the point of maximal temperature in the wake. The data is from the case with equilibrium chemistry. The contour lines show the temperatures 1400, 1500, 1600 and 1680 K. The top plot is from a slice at constant  $x=0.0639\text{m}$ , the middle at constant  $z=0.00772\text{m}$  and the bottom one at constant  $y=0.00366\text{m}$  from the lower front corner.

case it is an initial approach. The solver uses periodic boundary conditions in the spanwise direction. To adapt the flowfields that are (quasi-)symmetric but not periodic in the spanwise direction, the primary state has been treated to give zero first and second spanwise derivatives at the computational domain's side boundaries for all flow variables (Groskopf *et al.* 2008). The stability analysis is done for one ( $y - z$ ) crosscut plane at a downstream position  $x = 0.1275$ , where  $x$  starts at the front edge of the element,

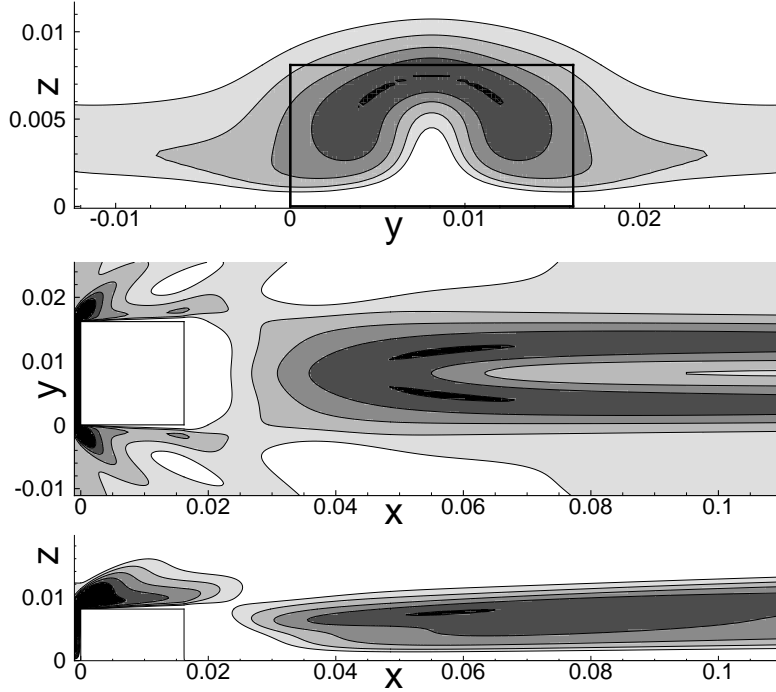


FIGURE 5. Similar to Fig. 4, but for the non-equilibrium case. The contour lines now show the temperature from 1400 through 1800 K in steps of 100 K and the slices are taken at constant  $x=0.0566\text{m}$ ,  $y=0.00115\text{m}$  and  $z=0.00746\text{m}$ .

---

Case	Temperature [K]	X [m]	Y [m]	Z [m]
Caloric	$1.86 \cdot 10^3$	$6.02 \cdot 10^{-2}$	$4.42 \cdot 10^{-3}$	$8.22 \cdot 10^{-3}$
Equilibrium	$1.69 \cdot 10^3$	$6.39 \cdot 10^{-2}$	$3.66 \cdot 10^{-3}$	$7.72 \cdot 10^{-3}$
Non-Equilibrium	$1.81 \cdot 10^3$	$5.66 \cdot 10^{-2}$	$1.15 \cdot 10^{-3}$	$7.46 \cdot 10^{-3}$

---

TABLE 2. Comparison of maximal temperatures in the wake of the cube for the different gas models. Reference for the location is the front, lower, right corner of the obstacle

corresponding to  $5.3\delta^*$  of the undisturbed flow past the roughness element that is  $\delta^* \approx 0.02\text{m}$  long and centered at  $R_{x,rough} \approx 565$ .

As the stability ansatz is temporal (index  $t$ ), yielding frequency  $\omega_{r,t}$  and temporal amplification rate  $\omega_{i,t}$  for a given streamwise spatial wavenumber  $\alpha_{r,t}$ , the amplification rates  $\alpha_i$  for the spatial approach are obtained applying Gaster's transformation according to Koch *et al.* (2000), see also Bonfigli & Kloker (2007):

$$\alpha_i = -\frac{\omega_{i,t}}{c_{gr,t}}, \quad (5.1)$$

where  $c_{gr,t}$  is the group velocity of the temporal approach. Furthermore, former investigations have shown that the group velocity can be well approximated by the phase velocity,  $c_{gr} \approx c_{ph}$ , see Bonfigli & Kloker (2007).

The spectra have been calculated for two streamwise wavenumbers. First, the wavenum-

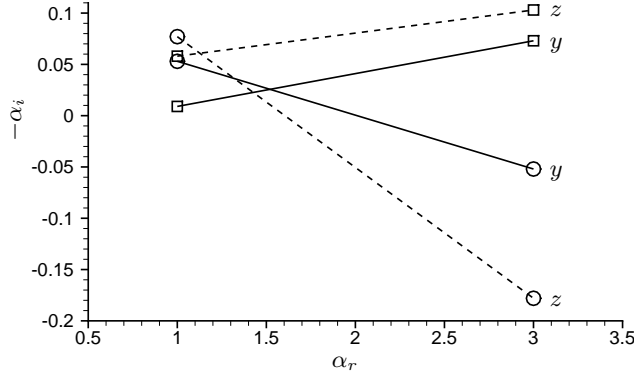


FIGURE 6. Spatial amplification rates over given streamwise wavenumbers indicated by symbols for the most amplified  $y$ -mode (solid lines) and  $z$ -mode (dashed lines) at  $x = 0.1275$  ( $R_x \approx 626$ ). Squares: calorically perfect primary, circles: equilibrium primary state.

ber is set to  $\alpha_{r,t} = \alpha_{r,t}^* \delta^* = 1.0$ , associated with first-mode instability in supersonic flat-plate boundary-layer flow. The second wavenumber chosen is  $\alpha_{r,t} = 3.0$  because it is assumed to be part of the regime where a second-/acoustic-mode instability can occur. Recall that for an acoustic mode  $\lambda^* = \frac{2\pi}{\alpha_{r,t}^*} \approx 2\delta^*$ .

From the obtained spectrum the most amplified physical eigenvalues and their corresponding eigenfunctions are isolated. Two different instability modes can be distinguished: The  $y$ -(or even) mode and  $z$ -(or odd) mode are related to wall-normal or spanwise shear in the primary-state flowfield, respectively.

Figure 6 displays the spatial amplification rates of the most amplified  $y$ - and  $z$ -mode for both streamwise wavenumbers and both flows. In the case of calorically perfect-gas flow the larger wavenumber ( $\alpha_{r,t} = 3.0$ ) is more amplified. The corresponding instability wave is supposed to be of acoustic-mode type. Higher amplification of the second mode is likely to be due to the strong wall cooling with  $T_{wall}$  being only 10% of the (too high) recovery temperature  $T_{rec}$ . In contrast, for the equilibrium flow first-mode instabilities ( $\alpha_{r,t} = 1.0$ ) are more unstable. The wall cooling at equal  $T_{wall}$  is much weaker, with  $T_{wall}$  now approximately  $0.22 T_{max}$  instead of  $0.14 T_{max}$  for the perfect-gas case, whereas  $y(T_{max})$  is virtually unaltered. The supersonic-disturbance region near the wall, where  $c_{ph} > u + a$ , is smaller in the equilibrium case because  $c_{ph}(z\text{-mode}) \approx 0.64$ , whereas  $c_{ph}(z\text{-mode}) \approx 0.75$  for the perfect-gas case.

This flow is too hot, leading to unduly large amplification rates for second-mode instabilities, which are pushed by the supersonic-disturbance region near the wall.

Comparing the two types of modes within both investigated flows, it is found that the  $z$ -mode is locally most unstable. For perfect-gas flow as well as in the case of chemical equilibrium the growth is by 40% larger than for the  $y$ -mode. Provided the streamwise evolution is like that observed by Groskopf *et al.* (2008) in a cold supersonic flow, where for distances larger than  $20\delta^*$  behind the roughness element the  $z$ -mode prevails, it will play the dominant role in the transition process. The reason is the development of streaks that induce larger  $\frac{\partial u}{\partial z}$  compared to  $\frac{\partial u}{\partial y}$ . Of course, the  $z$ -mode receptivity has to be as large as that for  $y$ -modes.

Figures 7 and 8 show the eigenfunctions of the streamwise velocity and tempera-

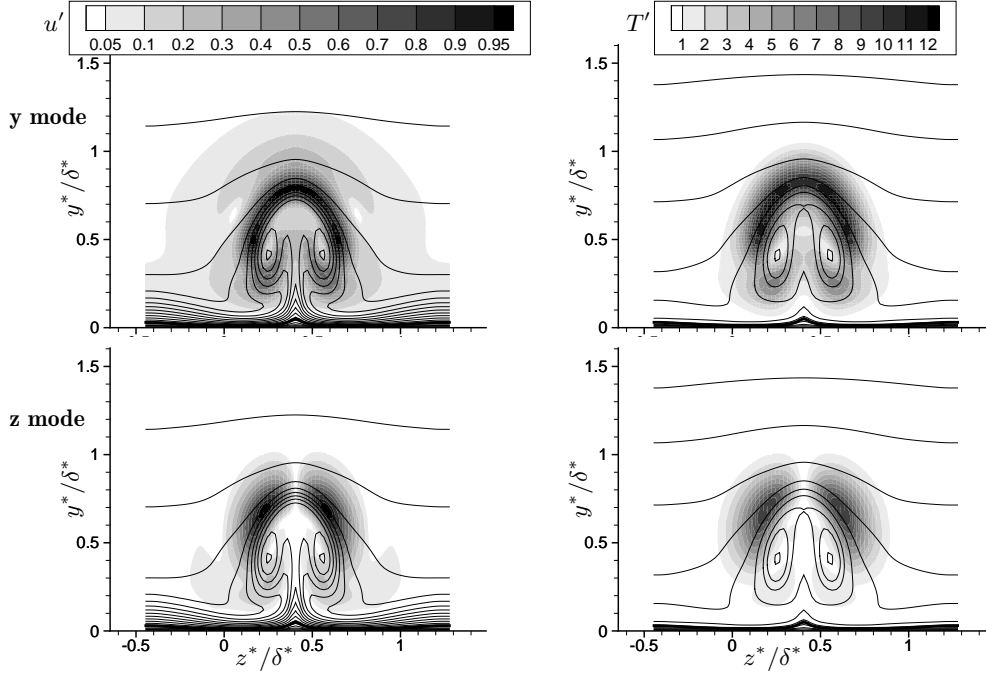


FIGURE 7. Calorically perfect primary state: modulus of the eigenfunctions of streamwise velocity  $u'$  (left) and temperature  $T'$  (right), normalized to  $u'_{max} = 1$ .  $y$ -mode (top) and  $z$ -mode (bottom) are displayed for  $\alpha_r = \alpha_r^* \delta^* = 3.0$ . Thin solid lines are isolines of  $u$  and  $T$ , respectively. The thick solid line marks the sonic line  $Ma = 1$  within the boundary layer for each case. The crosscut is situated at  $x = 0.1275$  ( $R_x \approx 626$ ), the roughness element at  $R_{x,rough} \approx 565$ . Phase velocities of the shown eigenmodes are in the range  $0.70 \leq c_{ph,t} \leq 0.75$ .

ture disturbances  $u'$ ,  $T'$  for the most amplified  $y$ - and  $z$ -mode of perfect-gas flow and equilibrium flow, respectively. The eigenfunctions have their maxima in regions of high primary-state gradients. For perfect-gas flow it can be seen that the ratio between the maximum amplitude of  $u'$  and  $T'$  reaches values of more than 12 for the  $y$ -mode owing to the unrealistically high temperatures. For the more amplified  $z$ -mode this ratio is lower than 10, which is still far too high though. For equilibrium flow (Fig. 8), however, the ratio does not exceed 3.5. Furthermore, the shapes of the  $u'$ -amplitudes of the  $y$ -mode as well as  $z$ -mode closely resemble those found by Groskopf *et al.* (2008) for the cold flow and a similar roughness setup, where the width of the element is  $2\delta^*$  instead of  $\delta^*$  considered here. The eigenfunctions resulting from the perfect-gas flow are rather distorted however.

Unexpectedly, the maximum growth rate at  $5\delta^*$  behind the roughness element in the hot equilibrium flow is markedly larger than in the cold Mach 4.8 case, whereas the associated streamwise wavenumber is about the same.

The stability code will be extended for allowing thermally perfect-gas flows in the near future to check for the accuracy of the results.

## 6. Conclusions

Direct numerical simulation in 2- and 3-D setups investigate mainly temperature and species development along the surface of the HyBoLT experimental setup. A cuboid-

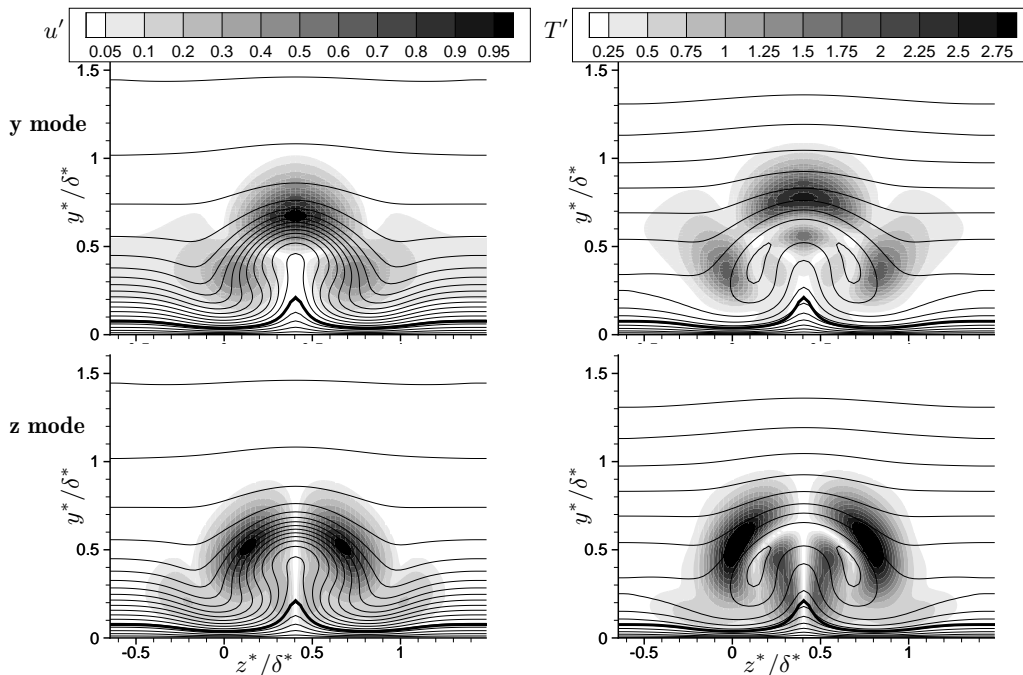


FIGURE 8. Same as Fig. 7, but for the equilibrium primary state, and for  $\alpha_r = 3.0$ ,  $0.64 \leq c_{ph,t} \leq 0.68$ .

shaped obstacle at about 500 mm from the virtual leading edge disturbs the flow, bringing high temperature gases closer to the surface through counter-rotating vortices in the direct wake. The horseshoe vortex does not show the same magnitude in heat-transfer rates and is therefore not described in detail in this work.

The 2-D simulations deliver the inflow and freestream conditions for the 3-D simulations in the direct vicinity of the obstacle. Separation regions upstream and downstream of the obstacle are much smaller in the 3-D simulations due to the proper representation of the horseshoe vortex.

The maximum temperatures in all three considered cases – caloric perfect gas, chemical equilibrium reaction and chemical non-equilibrium – are at the top-front edge of the sharp object leading to potential ablation. More noticeable for the design of the heat shield is the wake of the object. Here, the counter-rotating vortices transport high-temperature gases toward the surface leading to locally increased heat-transfer rates. The maximum temperatures in the caloric perfect gas are highest among the considered models as expected. Stepping to chemical equilibrium, dissociation diminishes maximum temperatures. For the chemical non-equilibrium case, maximum temperatures raise slightly, but more noticeable the location of the maximum moves closer to the wall leading to increased rates of heat transfer.

The stability investigations show unduly amplification for caloric perfect gas, most likely due to the strong gradients in the wall-normal temperature. In the chemically reacting flows, this gradient is diminished hand-in-hand with the decrease in maximum temperature, leading to amplification rates that are known from lower Mach number flows. The eigenfunctions in the caloric-perfect case are distorted whereas the eigenfunc-

tions in the chemical equilibrium case resemble modes known from a cold  $Ma=4.8$  case investigated by Groskopf *et al.* (2008).

Further investigations will include thermal non-equilibrium and more detailed investigation of wake properties.

### Acknowledgements

The authors thank O. Marxen and G. Iaccarino for the scientific support and S. Jones and S. Bedin for the organization and the technical help.

### REFERENCES

- BERRY S. A., FANG-JENQ C., WILDER M. C. & REDA D. C. 2007 Boundary layer transition experiments in support of the hypersonics program, AIAA-paper 2007-4266.
- BERRY, S. A. AND HORVATH, T. J. 2007 Discrete Roughness Transition for Hypersonic Flight Vehicles, AIAA paper 2007-307.
- BIRD, R. B., STEWART, W. E. & LIGHTFOOT, E. N. 1960 Transport Phenomena, John Wiley & Sons, New York.
- BLOTTNER, F. G., JOHNSON, M. & ELLIS, M. 1970 Chemically Reacting Viscous Flow Program for Multi Component Gas Mixture, Sandia Laboratories, SC-RR-70-754
- BONFIGLI, G. & KLOKER, M. J. 2007 Secondary instability of crossflow vortices: validation of the stability theory by direct numerical simulation. *J. Fluid Mech.* **583**, 229–272.
- GROSKOPF, G., KLOKER, M. J. & MARXEN, O. 2008 Bi-global secondary stability theory for high-speed boundary-layer flows. In *Proceedings of the 2008 Summer Program*, CTR, Stanford, CA, July 6–August 1.
- KOCH, W., BERTELOTTI, F. P., STOLTE, A. & HEIN, S. 2000 Nonlinear Equilibrium solutions in a three-dimensional boundary layer and their instability. *J. Fluid Mech.* **406**, 131–174.
- PARK, C. On Convergence of Chemical Reacting Flows, AIAA-paper 1985-0427.
- SCHNEIDER, S. P. 2007 Effects of Roughness on Hypersonic Boundary-Layer Transition, AIAA paper 2007-305.
- STEMMER, C. 2005 Hypersonic transition investigations in a flat-plate boundary layer-flow at  $M=20$ , AIAA-paper 2005-5136.
- TIRTEY, S. C., BOLNOT, H., BOTTINI, H., PARIS, S., FLETCHER, D. G. AND CHAZOT, O. 2008 In-Flight Hypersonic Roughness Induced Transition Experiment, AIAA 2008-250.
- VOS, J. B., LEYLAND, P., VAN KEMENADE, V., GACHERIEU, C., DUQUESNE, N., LOTSTEDT, P., WEBER, C., YTTERSTROM, A. & SAINT REQUIER, C. 2007 NSMB Handbook 4.5.
- VOS, J. B., BOHBOT, J., CHAMPAGNEUX, S., CORMIER, J., DARRACQ, D., KOZUCH, L., SOULERES, T., DUQUESNE, N., YTTERSTROM, A., SAINT REQUIER, C., LE MOIGNE, Y., GACHERIEU, C., PERSSON, I., SILLEN, M. & HOARAU, Y. 2006 NSMB 5.96 User Guide.
- WANG, X. & ZHONG, X. 2008 Receptivity of a Hypersonic Flat-Plate Boundary Layer to Surface Roughness, AIAA paper 2008-503.